

## Biohybrids of twinning Cd<sub>0.8</sub>Zn<sub>0.2</sub>S nanoparticles and *Sporomusa ovata* for efficient solar-driven reduction of CO<sub>2</sub> to acetate

Kejing Zhang<sup>a</sup>, Ruijie Li<sup>a</sup>, Jianxin Chen<sup>a</sup>, Liyuan Chai<sup>a,b,c</sup>, Zhang Lin<sup>a,b,c</sup>, Long Zou<sup>d,\*</sup>, Yan Shi<sup>a,b,c,\*\*</sup>

<sup>a</sup> School of Metallurgy and Environment, Central South University, Changsha 410083, China

<sup>b</sup> State Key Laboratory of Advanced Metallurgy for Non-ferrous Metals, Changsha 410083, China

<sup>c</sup> Chinese National Engineering Research Center for Control & Treatment of Heavy Metal Pollution, Changsha 410083, China

<sup>d</sup> College of Life Sciences, Jiangxi Normal University, Nanchang 330022, China



### ARTICLE INFO

#### Keywords:

Homojunctions  
Biohybrid catalyst  
Electron transfer  
CO<sub>2</sub> reduction

### ABSTRACT

Integration of microorganisms with semiconductors is an effective approach to sustainable solar-driven production of chemicals from CO<sub>2</sub>, which lies in the development of efficient, highly biocompatible, and low-cost photocatalysts. Herein, twinning Cd<sub>0.8</sub>Zn<sub>0.2</sub>S nanoparticles with long-range ordered homojunctions were synthesized and used for the first time in the construction of a biohybrid system (Cd<sub>0.8</sub>Zn<sub>0.2</sub>S/*S. ovata*) with a non-photosynthetic acetogenic bacterium of *Sporomusa ovata*. The Cd<sub>0.8</sub>Zn<sub>0.2</sub>S/*S. ovata* system yielded 49.33 ± 3.54 mM of acetate at a production rate of 8.22 ± 0.59 mM d<sup>-1</sup> with a quantum efficiency of 16.82 ± 1.21% under illumination, which exceeded those of other reported biotic-abiotic hybrid systems. Further investigations revealed that the twin-induced homojunctions with staggered phase alignment contributed to enhance the separation efficiency of photogenerated electron-hole pairs and avoid photocorrosion of the photocatalyst. Due to the dual advantages of light absorption and biocompatibility of Cd<sub>0.8</sub>Zn<sub>0.2</sub>S, the Cd<sub>0.8</sub>Zn<sub>0.2</sub>S/*S. ovata* system could efficiently harvest light energy and transfer photogenerated electrons to cellular metabolism, driving the Wood-Ljungdahl pathway to efficiently synthesize acetate from CO<sub>2</sub> under illumination.

### 1. Introduction

The consequence of excessive anthropogenic carbon emissions urgently requires the design of innovative strategies to develop carbon reduction and renewable energy technologies [1,2]. Photosynthesis is considered as one of the most desirable and sustainable strategies for CO<sub>2</sub> utilization. However, the naturally occurring transduction of solar energy into chemical bonds is too sluggish to keep pace with the needs of the modern society [3,4]. With advances in materials science, the quantum efficiency of the synthetic semiconductor photocatalysts often exceeds that of natural photosynthesis, but the artificial catalysts still struggle to replicate the complex C-C bond formation process mediated by living organisms for the selective production of multi-carbon products [1,5–9]. In recent years, the biohybrid systems integrating microorganisms with man-made semiconductors offer new opportunities for the solar-driven CO<sub>2</sub>-to-chemical conversion by taking advantages of both photo- and bio-catalysis [10–13]. To improve the performance of

the artificial photosynthetic system, there is an urgent need for ideal photocatalysts with suitable band gap for visible light absorption, sufficient reductive potential of the conduction band electrons for bio-catalysis, and high biocompatibility for bacterial growth.

Over the past few years, the CdS with a band gap of ca. 2.4 eV is one of the most prominent photocatalysts in the development of biohybrid systems because of its high visible light harvesting capacity, good charge carrier mobility, and suitable band edge potentials [14–17]. However, the chemical-producing rates of the biohybrid systems based on pristine CdS are still unsatisfactory owing to the rapid recombination of photogenerated electron-hole pairs and high energy barrier at surface sites [18,19]. In addition, the release of Cd<sup>2+</sup> caused by intrinsic photocorrosion could interfere with the biocatalytic process by replacing the metal core of functional enzymes, and even lead to toxic effects on living cells, thereby affecting the sustainability of CO<sub>2</sub> conversion by the biohybrid systems [20]. Therefore, it is desired to overcome the inherent limitations of pristine CdS through regulating its optical property to

\* Corresponding author.

\*\* Corresponding author at: School of Metallurgy and Environment, Central South University, Changsha 410083, China.

E-mail addresses: [zoulong@jxnu.edu.cn](mailto:zoulong@jxnu.edu.cn) (L. Zou), [shiyzyrs@csu.edu.cn](mailto:shiyzyrs@csu.edu.cn) (Y. Shi).

improve the photosynthetic activity and stability of biohybrid systems.

Currently, some strategies, including heterojunction constructing, heteroatom doping, and defect engineering, have been investigated for successfully tuning the features and activities of transition metal sulfide photocatalysts [21–23]. Thereinto, constructing heterojunctions at the nanoscale through the introduction of heteroatoms has been proved as an effective route to optimize electron transfer pathway and promote separation of photogenerated electron-hole pairs [21,24,25]. However, it remains a great challenge to precisely tailor the heterojunctions in composite photocatalysts to obtain the band structure of semiconductors that meet the needs of photosynthetic application [26]. Noteworthily, the twin-induced homojunctions in solid solutions has recently emerged as a type of structure that enables efficient separation of the photo-generated electron-hole pairs [27]. Specifically, as planar defects formed within monocrystalline semiconductor, twin boundaries occur periodically with a constant spacing and long-range order, resulting in the generation of myriad homojunctions in a specific dimension [28–30]. In particular, the electrical resistivity of crystals with high proportion of homojunctions is approximately one order of magnitude lower than that of crystals with routine grain boundaries, thus promoting the transfer of photogenerated carriers within a single crystalline photocatalyst [31]. Moreover, due to its self-building electrostatic field, the enrichment of photogenerated holes could be alleviated [28], thus enabling effective avoidance of metal leaching caused by photo-corrosion [32]. More importantly, the twin engineering does not require doping or combination of additional elements, which allows us to tune the band structure of semiconductors in a highly precise manner for specific applications. Therefore, twin engineering is expected to improve the photocatalytic activity and stability of metal sulfide, providing ideal photocatalysts for development of the artificial photosynthetic system. Nevertheless, constructing homojunctions with near periodic and dense distribution by adjusting the bridging mode of crystal phase in metal sulfide for boosting photosynthesis of biohybrid systems has rarely been reported until now.

Considering that CdZnS is one of the most typical semiconductor substrates for twin formation [27,33], the Cd<sub>x</sub>Zn<sub>1-x</sub>Ss with controllable optical and photoelectric properties were synthesized and applied, for the first time, to the construction of biohybrid systems in this study. Specifically, the unique twin-induced homojunctions with a long-range order were constructed in the Cd<sub>0.8</sub>Zn<sub>0.2</sub>S nanoparticles (NPs) by a hydrothermal method. The synthesized Cd<sub>0.8</sub>Zn<sub>0.2</sub>S NPs were used as photosensitizers to integrate *Sporomusa ovata* (*S. ovata*), a model acetogenic bacterium [34–36], into a biohybrid system (Cd<sub>0.8</sub>Zn<sub>0.2</sub>S/S. *ovata*) for light-driven CO<sub>2</sub> conversion. The photosynthetic performance of the as-prepared Cd<sub>0.8</sub>Zn<sub>0.2</sub>S/S. *ovata* system was systematically evaluated. As expected, it exhibited a superior photosynthetic acetate production activity and stability. The electron generation and transfer in the Cd<sub>0.8</sub>Zn<sub>0.2</sub>S/S. *ovata* system were discussed according to various characterizations and density functional theory (DFT) calculations. Moreover, the transcriptome profiles of *S. ovata* in the Cd<sub>0.8</sub>Zn<sub>0.2</sub>S/S. *ovata* system in response to light exposure were analyzed to elucidate the underlying molecular mechanism of photosynthesis. This study provided new insights into the design of high-performance artificial photosynthesis platforms for the reduction of CO<sub>2</sub> into chemicals.

## 2. Materials and methods

### 2.1. Synthesis of the Cd<sub>x</sub>Zn<sub>1-x</sub>S

The twinning Cd<sub>x</sub>Zn<sub>1-x</sub>Ss (x = 0.2, 0.4, 0.6, and 0.8) were synthesized via a simple hydrothermal method. At room temperature, (n) mmol of Cd(Ac)<sub>2</sub>·2 H<sub>2</sub>O (n = 2, 4, 6, and 8) and (10-n) mmol of Zn (Ac)<sub>2</sub>·2 H<sub>2</sub>O were dissolved in 70 mL of deionized water under constant magnetic stirring. Then, 30 mL of fresh Na<sub>2</sub>S solution (10 mmol) was slowly added using a micro-injection pump in 30 min for the deposition

of the metal ions. After stirring for 2 h, the obtained yellowish precursor solution was transferred into a 200 mL of Teflon-lined autoclave and maintained at 180 °C for 12 h. The precipitates harvested by centrifugation at 8000 rpm for 5 min were washed several times with deionized water and ethanol, and dried at 60 °C for 10 h. The final obtained samples were named as Cd<sub>x</sub>Zn<sub>1-x</sub>S. Bulk phases of CdS and ZnS were synthesized using the same procedures using Cd(Ac)<sub>2</sub>·2 H<sub>2</sub>O and Zn (Ac)<sub>2</sub>·2 H<sub>2</sub>O, respectively, with Na<sub>2</sub>S·9 H<sub>2</sub>O in a molar ratio of Cd/Zn:S = 1:1.

### 2.2. Construction of Cd<sub>0.8</sub>Zn<sub>0.2</sub>S/S. *ovata* biohybrid

*S. ovata* DSM 2662 was purchased from Mingzhou Biotechnology Co., Ltd (Ningbo, China). All culture and sampling manipulations were performed in an anaerobic glovebox with a mixed gas atmosphere of N<sub>2</sub>/CO<sub>2</sub> (1.5 atm, 80:20, v/v). *S. ovata* was grown in a sterilized medium (Table S1) that was modified based on ATCC Culture Medium 1425. When the growth stage of *S. ovata* reached the logarithmic phase (OD<sub>545</sub> = 0.25), Cd<sub>0.8</sub>Zn<sub>0.2</sub>S was added into the medium to the final concentration of 0.5 mM. After 8 h of cultivation at a magnetic stirring speed of 150 rpm, the medium was sequentially centrifuged at the speed of 8000 rpm for 5 min. The harvested Cd<sub>0.8</sub>Zn<sub>0.2</sub>S/S. *ovata* biohybrids were thoroughly washed with sterile water three times for further use. The CdS/S. *ovata* and ZnS/S. *ovata* biohybrids were prepared by the same method as controls.

### 2.3. Photosynthesis reaction

Each biohybrid resuspended with 50 mL of sterilized photosynthetic medium (Table S2) was added into a 125 mL of serum bottle. Cysteine (0.25 wt%) was selected as a sacrificial agent to quench the hole pair. Each bottle was magnetically stirred (120 rpm) at 30 °C and irradiated by an in-house fabricated circular LED array composed of violet LEDs (450 ± 5 nm) for blue light measurements at a light intensity of 20 W m<sup>-2</sup>.

### 2.4. Measurement of the photosynthetic products

The photosynthetic products were analyzed by proton nuclear magnetic resonance (<sup>1</sup>H NMR, 500 M Avance III spectrometer, Bruker, Germany) spectroscopy with sodium 3-(trimethylsilyl)-2,2',3,3'-tetra-deuteropropionate (TMSP-d4) as the internal standard. The <sup>13</sup>C-isotope labeling experiment was conducted in the Cd<sub>0.8</sub>Zn<sub>0.2</sub>S/S. *ovata* system with NaH<sup>13</sup>CO<sub>3</sub> as sole carbon source.

The quantum efficiency was determined by the ratio of the effective electrons used for acetate production to the measured photon flux. The reduction of two CO<sub>2</sub> molecules to one acetate molecule requires 8 electrons, giving the following quantum efficiency (QE) equation:

$$\text{QE}(\%) = \frac{8 \times C_a \times V \times N_A}{\Phi_{ph} \times t \times A} \times 100\%$$

Where.

C<sub>a</sub> = total acetate concentration (mol).

V = total suspension volume.

Φ<sub>ph</sub> (cm<sup>-2</sup> s<sup>-1</sup>) = photo flux.

A (cm<sup>2</sup>) = area of illumination.

t (s) = reaction time (t).

N<sub>A</sub> = Avogadro's Number (6.022 × 10<sup>23</sup>).

### 2.5. Characterization

Detailed information was provided in the Supporting Information.

## 2.6. Transcriptomic analysis

Triplicate *S. ovata* cells were harvested from the  $\text{Cd}_{0.8}\text{Zn}_{0.2}\text{S}/\text{S. ovata}$  system (marked as the Light) and heterotrophic cultures with addition of betaine (marked as the Control), respectively. The RNA preparation, library construction, and sequencing on a BGISEQ-500 platform were performed at the BGI Genomics Institute. The transcriptomic data were analyzed according to the previous reports [37].

## 3. Results and discussion

### 3.1. Characterization of the $\text{Cd}_{0.8}\text{Zn}_{0.2}\text{S}/\text{S. ovata}$ system

The construction and performance of  $\text{Cd}_x\text{Zn}_{1-x}\text{S}/\text{S. ovata}$  system for photosynthesis were briefly described in Fig. 1a. Firstly, the  $\text{Cd}_x\text{Zn}_{1-x}\text{S}$  semiconductors were synthesized by the hydrothermal reaction of corresponding metal ions. The actual molar ratios of Cd and Zn elements in the samples were detected by inductively coupled plasma mass

spectrometry (ICP-MS), which were close to the additive proportion (Table S3). The crystal structures of all prepared samples were analyzed by X-ray diffraction (XRD). As shown in Fig. 1b, the bulk phase of ZnS was identified as the typical cubic (PDF#77-2100), while the bulk phase of CdS was identified as a mixture of the cubic and hexagonal (PDF#89-0440 and PDF#01-0780) [33,38]. It is worth noting that the XRD features of  $\text{Cd}_x\text{Zn}_{1-x}\text{S}$  gradually and consistently shifted from those of ZnS to CdS as the Cd content increased, demonstrating the successful formation of solid solutions in  $\text{Cd}_x\text{Zn}_{1-x}\text{S}$  (Fig. S1). The characteristics of multiphase in  $\text{Cd}_x\text{Zn}_{1-x}\text{S}$  suggested the possible formation of wurtzite-spahelerite phase-junctions [33]. Furthermore, scanning electron microscopy (SEM) and transmission electron microscopy (TEM) images were recorded to characterize the morphology and microstructure of  $\text{Cd}_x\text{Zn}_{1-x}\text{S}$ . SEM image of the optimized  $\text{Cd}_{0.8}\text{Zn}_{0.2}\text{S}$  (demonstrated in the following part) revealed the uniform morphology of NPs (Fig. 1c). Moreover, the corresponding energy dispersive X-ray spectrometry (EDS) elemental mappings identified the homogeneous distributions of Cd, Zn, and S (Fig. 1c). Low magnification TEM image

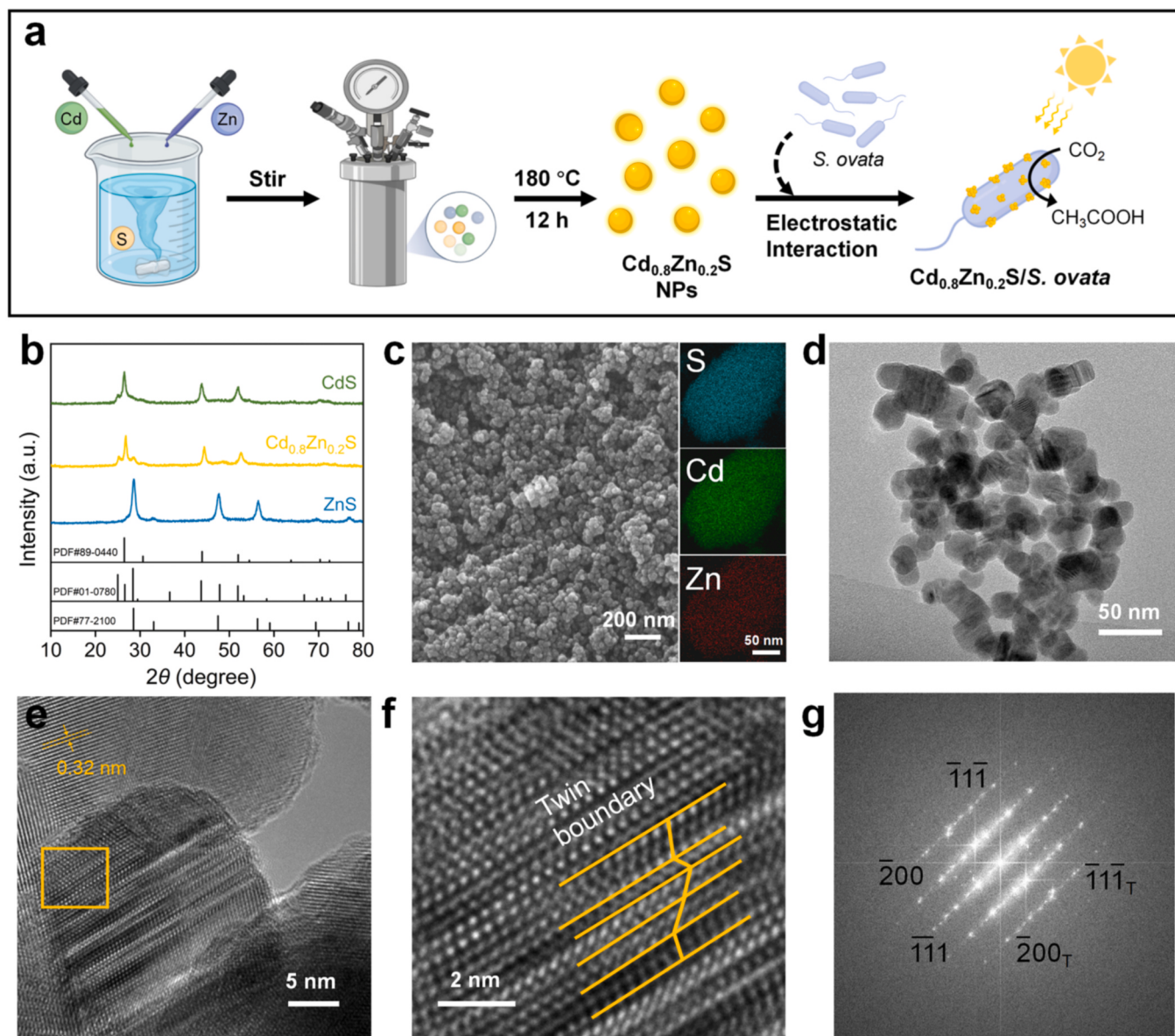


**Fig. 1.** (a) Schematic illustration for the construction of the  $\text{Cd}_{0.8}\text{Zn}_{0.2}\text{S}/\text{S. ovata}$  system. (b) XRD patterns of the CdS, ZnS, and  $\text{Cd}_{0.8}\text{Zn}_{0.2}\text{S}$ . (c) SEM image and the corresponding EDS element (S, Cd, and Zn) mappings of the  $\text{Cd}_{0.8}\text{Zn}_{0.2}\text{S}$ . TEM (d) and HRTEM images (e, f) of the  $\text{Cd}_{0.8}\text{Zn}_{0.2}\text{S}$ . (g) The SAED pattern of twin boundary in the  $\text{Cd}_{0.8}\text{Zn}_{0.2}\text{S}$ .

(Fig. 1d) showed consecutively distributed  $\text{Cd}_{0.8}\text{Zn}_{0.2}\text{S}$  NPs with well-proportioned particle size (20–30 nm). High resolution TEM (HRTEM) image showed the lattice spacing of 0.32 nm, which corresponds to (111) plane of zinc-blende lattice (Fig. 1e) [39]. The abundant existence of zigzag structures and parallel dislocations composed of coherent twin boundaries indicated the twin crystal structures (Fig. 1f). The formation of the nanoscale twin crystal structure was also supported by the unique diffraction features from the selected area electron diffraction (SAED) pattern (Fig. 1g), wherein ordered spots appearing at the sites one-third from the normal spots were attributed to the deviated atoms after twinning from the original sites [26,40]. These results substantially confirmed the formation of solid solutions and excluded the possibility of phase segregation between CdS and ZnS in the  $\text{Cd}_{0.8}\text{Zn}_{0.2}\text{S}$  NPs.

X-ray photoelectron spectroscopy (XPS) high-resolution spectra of Cd 3d, Zn 2p, and S 2p were analyzed to reveal the chemical environment of the elements (Fig. S2). With the increase of Cd/Zn ratio, the binding energy of Cd 3d and S 2p gradually shifted towards that of pure CdS, which suggested the formation of Cd-S bonds in the  $\text{Cd}_x\text{Zn}_{1-x}\text{S}$  NPs. Meanwhile, Zn 2p peaks also negatively shifted, indicating that valence electrons were drawn by the CdS component. This probably favored the photocatalytic performance of  $\text{Cd}_x\text{Zn}_{1-x}\text{S}$  in the range of visible light [22,41]. The optical absorption properties of the  $\text{Cd}_x\text{Zn}_{1-x}\text{S}$ s were investigated by UV-vis diffuse reflection spectroscopy (UV-Vis DRS). The ZnS showed a narrow UV absorption range, while CdS displayed a broad visible light absorption range from ca. 400–600 nm (Fig. S3). In  $\text{Cd}_x\text{Zn}_{1-x}\text{S}$ s, the presence of Cd led to the red shifts of the absorption edges from ca. 500–600 nm, suggesting that these solid solutions were endowed with characteristics of response to

the visible light. The measured direct band gaps of  $\text{Cd}_x\text{Zn}_{1-x}\text{S}$ s were in a range from 2.33 to 2.49 eV (Fig. S4 and Table S4), which were between that of pure CdS (2.12 eV) and ZnS (3.39 eV). It demonstrated that the light absorption capacities of  $\text{Cd}_x\text{Zn}_{1-x}\text{S}$  were readily controlled by adjusting the Cd/Zn molar ratios.

For a semiconductor photocatalyst used in the artificial photosynthesis systems, it is critical to increase the generation rate of electron-hole pairs and the half-life of the generated electrons. Photoelectrochemical tests demonstrated that the  $\text{Cd}_{0.8}\text{Zn}_{0.2}\text{S}$  possessed the highest electron-hole pair yield compared with other  $\text{Cd}_x\text{Zn}_{1-x}\text{S}$ s (Fig. S5a), accordingly, the  $\text{Cd}_{0.8}\text{Zn}_{0.2}\text{S}$  showed the best photocatalytic acetate production in the biohybrid system (Fig. S5b). Based on this, the  $\text{Cd}_{0.8}\text{Zn}_{0.2}\text{S}$  photosensitizer was applied to incubate with *S. ovata* for construction of the  $\text{Cd}_{0.8}\text{Zn}_{0.2}\text{S}/\text{S. ovata}$  system (Fig. 1a). The zeta potential of *S. ovata* suspension was positively shifted from –38.17 to –32.67 mV after hybridizing  $\text{Cd}_{0.8}\text{Zn}_{0.2}\text{S}$  NPs with a positive potential of 25.32 mV, indicating that  $\text{Cd}_{0.8}\text{Zn}_{0.2}\text{S}$  NPs accumulated on the surface of *S. ovata* through electrostatic interactions. XRD patterns of the developed biohybrids further suggested the successful assembly of different photocatalysts on *S. ovata* without detectable changes in their phase structures (Fig. 2a). SEM, TEM and TEM-EDS elemental mapping images showed that the  $\text{Cd}_{0.8}\text{Zn}_{0.2}\text{S}$  NPs were bound to the cell surface of *S. ovata* in clustered or dispersed form (Fig. 2b-d), while these bacterial cells retained their initial sizes and shapes (Fig. S6), suggesting a good biocompatibility of the  $\text{Cd}_{0.8}\text{Zn}_{0.2}\text{S}$  NPs to *S. ovata*. It was further confirmed by the unaffected growth kinetic of *S. ovata* in the  $\text{Cd}_{0.8}\text{Zn}_{0.2}\text{S}/\text{S. ovata}$  system (Fig. S7). The metal leaching results showed that no metal ions were characterized after 24 h of illumination (Table S5). In addition, SEM and XRD results indicated that the

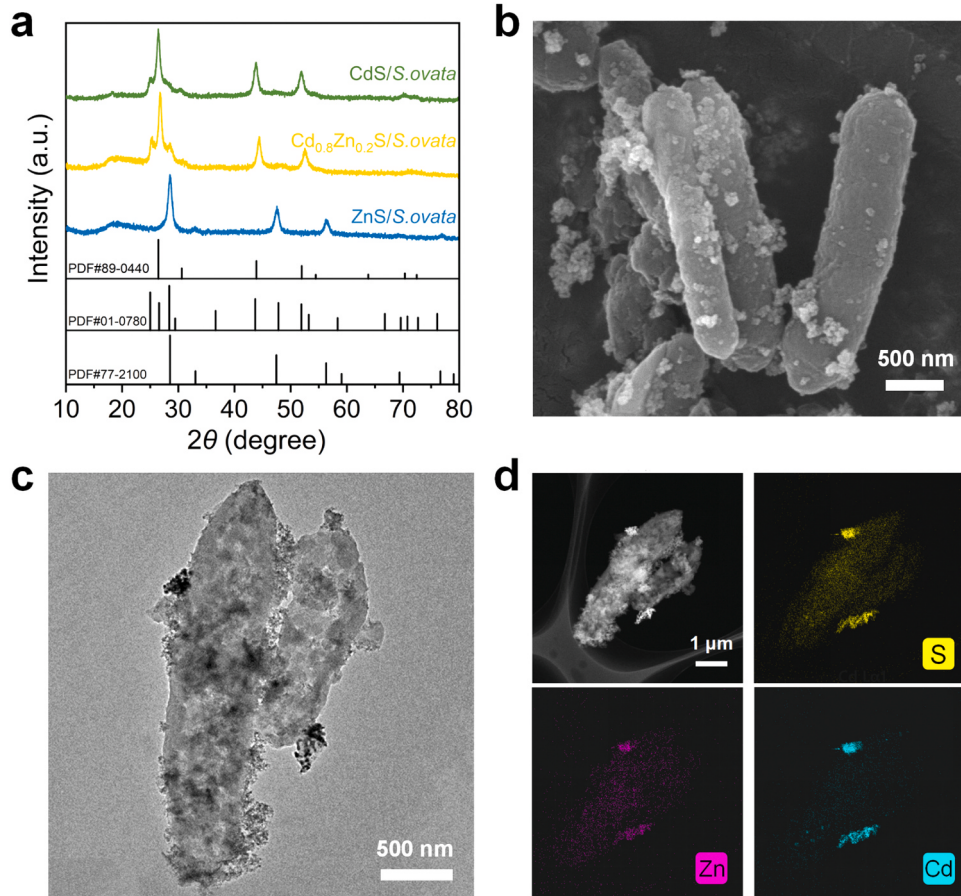


**Fig. 2.** (a) XRD patterns of the  $\text{CdS}/\text{S. ovata}$ ,  $\text{ZnS}/\text{S. ovata}$ , and  $\text{Cd}_{0.8}\text{Zn}_{0.2}\text{S}/\text{S. ovata}$  biohybrids. SEM (b), TEM (c), and TEM-EDS elemental mapping (d) images of the  $\text{Cd}_{0.8}\text{Zn}_{0.2}\text{S}/\text{S. ovata}$  biohybrids.

$\text{Cd}_{0.8}\text{Zn}_{0.2}\text{S}/\text{S. ovata}$  biohybrids still maintained its initial structural characteristics after illumination (Fig. S8 and S9). These demonstrated a great stability of  $\text{Cd}_{0.8}\text{Zn}_{0.2}\text{S}$  in the biohybrid system. Compared to the photocorrosion prevalent in monometallics, bimetallic sulfur-bridge bonds effectively inhibit metal leaching that could lead to reduced biocatalytic activity [20,42]. These evidences suggested the successful construction of a stable photo-responsive  $\text{Cd}_{0.8}\text{Zn}_{0.2}\text{S}/\text{S. ovata}$  system, in which *S. ovata* has a potential to realize  $\text{CO}_2$  conversion through harvesting photoexcited electrons from the  $\text{Cd}_{0.8}\text{Zn}_{0.2}\text{S}$  NPs under illumination (Fig. 1a).

### 3.2. Photosynthesis of the $\text{Cd}_{0.8}\text{Zn}_{0.2}\text{S}/\text{S. ovata}$ system

To investigate photosynthesis of the  $\text{Cd}_{0.8}\text{Zn}_{0.2}\text{S}/\text{S. ovata}$  system, the prepared biohybrids were cultivated under the irradiation of LED light source ( $450 \pm 5 \text{ nm}$ ) at  $35 \pm 2 \text{ }^\circ\text{C}$ . Cell numbers determined by colony-forming unit (CFU) assays suggested that *S. ovata* in the biohybrid systems required light to maintain their viability (Fig. S10). Furthermore, compared to the biohybrid systems, the rapid decline in survival rate of bare *S. ovata* under light-exposure condition indicated the protective effect of photosensitizers on bacteria [10,37]. As expected, only the biohybrid systems composed of living bacterial cells and photosensitizers ( $\text{CdS}$ ,  $\text{ZnS}$  or  $\text{Cd}_{0.8}\text{Zn}_{0.2}\text{S}$ ) could produce acetate in the presence of  $\text{CO}_2$  under illumination (Fig. 3a). The acetate yield in the  $\text{Cd}_{0.8}\text{Zn}_{0.2}\text{S}/\text{S. ovata}$  system ( $35.20 \pm 3.28 \text{ mM}$ ) was significantly higher than those in the  $\text{CdS}/\text{S. ovata}$  ( $26.20 \pm 1.33 \text{ mM}$ ) and  $\text{ZnS}/\text{S. ovata}$  ( $18.69 \pm 3.28 \text{ mM}$ ) system under the same conditions, probably owing to high generation rate of electron-hole pairs and good affinity of the  $\text{Cd}_{0.8}\text{Zn}_{0.2}\text{S}$ . Moreover, the  $^1\text{H}$  NMR spectra revealed that only acetate

was produced in the conversion of  $\text{CO}_2$ , which was attributed to the highly selective  $\text{CO}_2$  fixation pathway employed by *S. ovata* (Fig. S11). Specifically,  $\text{CO}_2$  was reduced intracellularly to a common biosynthetic intermediate of acetyl coenzyme A, which was ultimately converted to acetic acid as a metabolic waste product and excreted from the cell [43]. Isotope-labeling experiments further demonstrated that the acetate produced by the  $\text{Cd}_{0.8}\text{Zn}_{0.2}\text{S}/\text{S. ovata}$  system was derived from  $\text{CO}_2$  reduction (Fig. 3b).

The effects of photosensitizer concentration and illumination intensity on the photosynthetic efficiency in the  $\text{Cd}_{0.8}\text{Zn}_{0.2}\text{S}/\text{S. ovata}$  system were investigated. Within a certain range, increasing the photosensitizer concentration could provide more photoelectrons to drive the  $\text{CO}_2$  fixation in bacterial cells, however, when the concentration of photosensitizer exceeded the threshold (0.5 mM), the acetate production was inhibited (Fig. 3c). On the other hand, the illumination intensity was also critical for the biohybrid systems to perform photosynthesis. Low power density limited the production rate of photo-generated hole-electron pairs, while excessive illumination intensity might lead to the oxidative photodamage to bacterial cells, thus hindering the photosynthetic reaction and subsequently reducing the acetate yield (Fig. S12). A maximum acetate yield of  $43.46 \pm 2.57 \text{ mM}$  was achieved under the optimal condition ( $\text{Cd}_{0.8}\text{Zn}_{0.2}\text{S}$  dosage of 0.5 mM and a light intensity of  $70 \text{ W m}^{-2}$ ). To further evaluate the practicability of the  $\text{Cd}_{0.8}\text{Zn}_{0.2}\text{S}/\text{S. ovata}$  system, it was illuminated at a low light intensity ( $20 \text{ W m}^{-2}$ ) with successive light/dark (12/12 h) cycles to simulate natural light irradiation (Fig. 3d). Acetate was continuously produced during the light/dark cycles due to the accumulation of metabolic intermediates [19,44]. The turnaround in the rate of acetate production on the second day was attributed to the adaptation process of

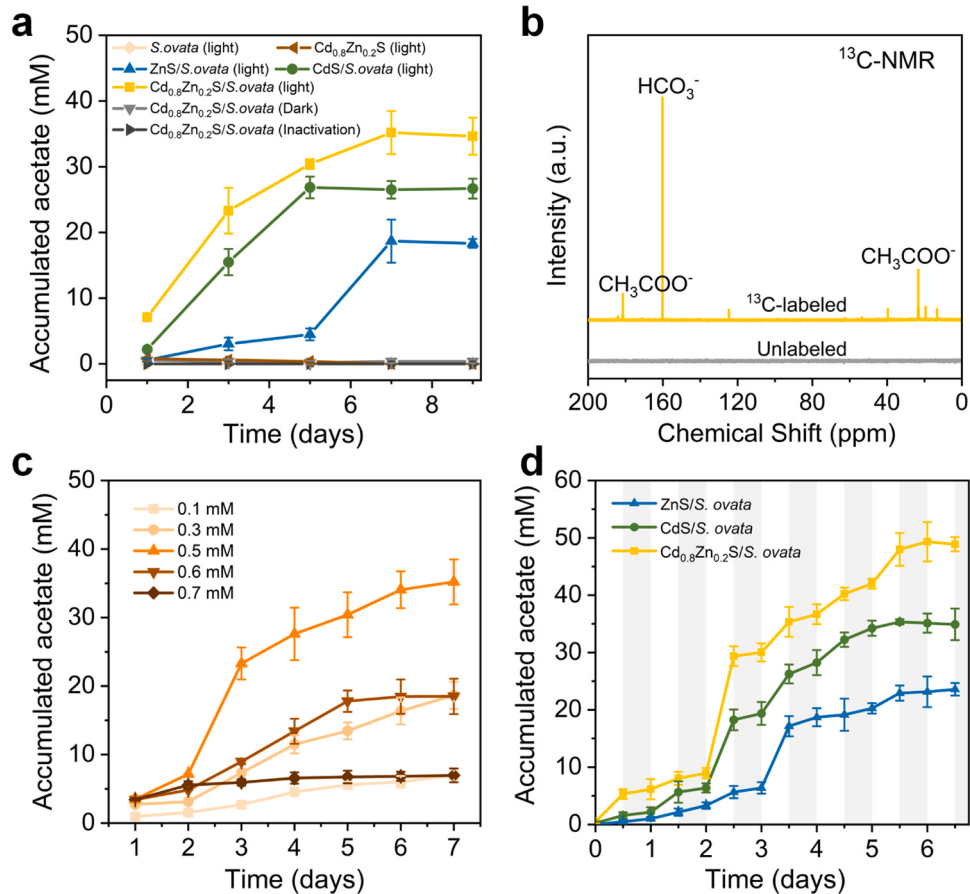


**Fig. 3.** (a) The yields of acetate in the  $\text{CdS}/\text{S. ovata}$ ,  $\text{ZnS}/\text{S. ovata}$ ,  $\text{Cd}_{0.8}\text{Zn}_{0.2}\text{S}/\text{S. ovata}$ , and deletional systems. (b)  $^{13}\text{C}$ -NMR spectra of the produced acetate with and without  $\text{NaH}^{13}\text{CO}_3$  as carbon source. (c) The yields of acetate in the  $\text{Cd}_{0.8}\text{Zn}_{0.2}\text{S}/\text{S. ovata}$  system with different  $\text{Cd}_{0.8}\text{Zn}_{0.2}\text{S}$  contents. (d) The yields of acetate in the  $\text{CdS}/\text{S. ovata}$ ,  $\text{ZnS}/\text{S. ovata}$ , and  $\text{Cd}_{0.8}\text{Zn}_{0.2}\text{S}/\text{S. ovata}$  systems under a continuous light/dark cycle of 12 h.

the bacteria from heterotrophy to photoautotrophy, which was further supported by the corresponding increase in cell viability (Fig. S13). The yield of acetate began to plateau on the sixth day, because of the limited amounts of the sacrificial hole scavenger [19,44]. The maximum yield of acetate reached  $49.33 \pm 3.54$  mM. Notably, the acetate production rate ( $8.22 \pm 0.59$  mM d<sup>-1</sup>) was substantially higher than that of other acetate-producing biohybrid systems (Table S6). In addition, the quantum yield of  $16.82 \pm 1.21\%$  was obtained, which exceeded the reported photosynthetic biotic-abiotic hybrid systems (1.6–12.4%) [6,10,44,45]. Multi-cycle experiments showed that the acetate production rate of the Cd<sub>0.8</sub>Zn<sub>0.2</sub>S/S. ovata system was well maintained over three 6-day cycles (Fig. S14), suggesting its potential for practical applications.

### 3.3. Twin engineering improved the photoelectron separation and transfer efficiency

To understand the mechanism underlying the excellent performance of the Cd<sub>0.8</sub>Zn<sub>0.2</sub>S/S. ovata system, the photoelectrochemical property of Cd<sub>0.8</sub>Zn<sub>0.2</sub>S, which governs photoelectron separation and transfer, was first evaluated, compared with CdS and ZnS. As shown in Fig. 4a, the Mott-Schottky plots of CdS, ZnS, and Cd<sub>0.8</sub>Zn<sub>0.2</sub>S presented positive slopes, proving their n-type semiconductor characteristics [16]. The slope of Cd<sub>0.8</sub>Zn<sub>0.2</sub>S was lower than that of CdS and ZnS, indicating an increase in the charge carrier density [16,46]. The high donor density of Cd<sub>0.8</sub>Zn<sub>0.2</sub>S demonstrated the dramatically improved charge separation efficiency and electrical conductance because of the twin crystal structure. Moreover, the obviously positive flat-band voltage ( $E_{fb}$ ) value of the Cd<sub>0.8</sub>Zn<sub>0.2</sub>S indicated a less electron-trapping process and higher quantum efficiency compared to the pure CdS and ZnS (Fig. 4a) [47]. To further reveal the photosensitizing behavior of Cd<sub>0.8</sub>Zn<sub>0.2</sub>S, photoluminescence (PL) spectroscopy was performed. The pure ZnS exhibited a strong PL emission peak centered at 535 nm due to the charge

recombination induced by surface-defect (Fig. S15) [48]. In comparison, the PL emission spectra of the twinning Cd<sub>0.8</sub>Zn<sub>0.2</sub>S and pure CdS gave broad peaks with red shifts, which were originated from the trap-level emissions [21]. In addition, the significant decrease in PL intensity of Cd<sub>0.8</sub>Zn<sub>0.2</sub>S indicated that the photo-induced carrier recombination was effectively inhibited [49]. Time-resolved photoluminescence (TR-PL) decay spectra (Fig. 4b) were obtained to evaluate the charge separation efficiency. The average PL lifetime values ( $\tau_{ave}$ ) of Cd<sub>0.8</sub>Zn<sub>0.2</sub>S, CdS, and ZnS were calculated to be 71.79, 40.61, and 59.70 ns, respectively (Table S7). The high efficiency of photoelectron separation on the surface of Cd<sub>0.8</sub>Zn<sub>0.2</sub>S was beneficial for electron transfer from the light-excited Cd<sub>0.8</sub>Zn<sub>0.2</sub>S to the energy harvesting system of S. ovata. These results were further corroborated by the chronoamperometric I-T curves with repetitive on/off cycles of irradiation, where the Cd<sub>0.8</sub>Zn<sub>0.2</sub>S/S. ovata biohybrid showed substantially higher photocurrent intensity than the CdS/S. ovata and ZnS/S. ovata biohybrids (Fig. 4c). Moreover, the current of CdS/S. ovata biohybrid decreased over time likely due to the rapid recombination of electrons and holes in the pure CdS [50]. This was in agreement with the PL results, in which the average PL lifetime of pure CdS was shorter than that of ZnS and Cd<sub>0.8</sub>Zn<sub>0.2</sub>S, suggesting a remarkable short-lived charge separation (Table S7). The Nyquist plots were obtained to analyze the charge transfer kinetics. The Cd<sub>0.8</sub>Zn<sub>0.2</sub>S/S. ovata exhibited a smaller interfacial resistance (Rct) compared to the CdS/S. ovata and ZnS/S. ovata, confirming a faster interfacial electron transfer in the Cd<sub>0.8</sub>Zn<sub>0.2</sub>S/S. ovata biohybrid under illumination (Fig. 4d). These results illustrated that the Cd<sub>0.8</sub>Zn<sub>0.2</sub>S with twin-induced homojunctions could effectively accelerate the generation and transfer of photoelectrons.

The energy level structure in Cd<sub>0.8</sub>Zn<sub>0.2</sub>S was investigated to better understand the behavior of electron transfer in the twinning structure. Based on above analysis, the structural configuration (Fig. 4e) and band position (Fig. 4f) for the twinning Cd<sub>0.8</sub>Zn<sub>0.2</sub>S were proposed. In general,

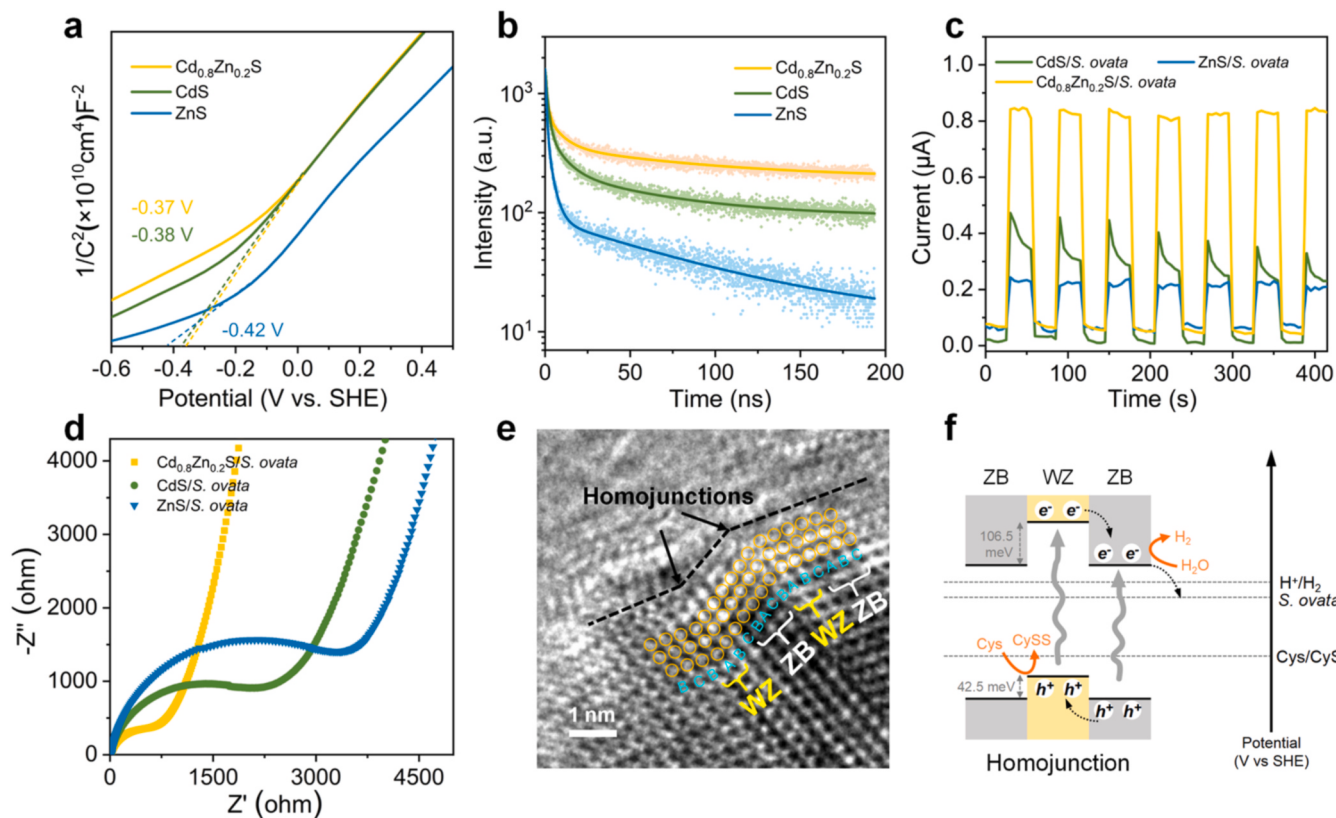


**Fig. 4.** Mott-Schottky plots (a) and TR-PL decay curves (b) of the CdS, ZnS, and Cd<sub>0.8</sub>Zn<sub>0.2</sub>S. (c) I-T curves of the CdS/S. ovata, ZnS/S. ovata, and Cd<sub>0.8</sub>Zn<sub>0.2</sub>S/S. ovata biohybrids under a light on/off cycle. (d) Nyquist plots of the CdS/S. ovata, ZnS/S. ovata, and Cd<sub>0.8</sub>Zn<sub>0.2</sub>S/S. ovata biohybrids. (e) Atomic scale image of twin-induced homojunctions in the Cd<sub>0.8</sub>Zn<sub>0.2</sub>S. (f) Mechanism for photogenerated charge separation in the homojunction of Cd<sub>0.8</sub>Zn<sub>0.2</sub>S. Cys, cysteine. Cyss, cystine.

binary compounds with close-packed crystal structures can crystallize into zinc-blende (ZB), wurtzite (WZ), and a mixture of them [27]. When stacking faults are introduced, the otherwise ordered ZB and WZ structures may be disrupted [26]. As shown in Fig. 4e, the misplacement of ZB layer in the (111) direction formed a twin plane with mirror-symmetric structures, in which the misaligned lattice sequences (e.g., BAB arrays) could be considered as a WZ structure [51,52]. As a result, the appearance of these twin planes in nanocrystals broke the continuous ZB lattice constitution and created numerous WZ segments [26]. Specifically, periodic light/dark contrast resulted from alternating twins along the (111) crystalline direction of Cd<sub>0.8</sub>Zn<sub>0.2</sub>S NPs could be clearly observed (Fig. 4e). Furthermore, the average band gap of the twinning Cd<sub>0.8</sub>Zn<sub>0.2</sub>S nanocrystals was determined to be 2.62 eV. The conduction band (CB) and valence band (VB) positions were calculated to be -0.579 and 1.751 eV (Fig. 4f), which could effectively drive photocatalytic hydrogen evolution (-0.41 V vs. SHE) [53] and cysteine oxidation (1.04 V vs. SHE) [54], respectively. More importantly, the WZ Cd<sub>0.8</sub>Zn<sub>0.2</sub>S was demonstrated to occupy higher CB and VB positions than its ZB counterpart [26,55]. Therefore, a large amount of homojunctions consisting of two phases (ZB and WZ) in the Cd<sub>0.8</sub>Zn<sub>0.2</sub>S

offered gradient built-in electric fields, resulting in highly efficient separation and migration of photogenerated electron-hole pairs (Fig. 4f).

To further elucidate the role of active sites in electron transfer at the biotic-abiotic interface, density functional theory (DFT) calculation was conducted. The DFT calculations of the energy band structure (Fig. 5a-c) and density of states (Fig. 5d-f) revealed the typical semiconductor features of CdS, ZnS, and Cd<sub>0.8</sub>Zn<sub>0.2</sub>S. The Cd<sub>0.8</sub>Zn<sub>0.2</sub>S possessed a significantly higher charge density than CdS and ZnS at the Fermi energy level, which contribute to an excellent conductivity. The differential charge density distribution in the Cd<sub>0.8</sub>Zn<sub>0.2</sub>S were showed in Fig. 5g, where the yellow and light blue parts represented charge accumulation and depletion, respectively. Apparently, the electrons in the region of S atoms were accumulated by the electron loss and transfer of on the Cd and Zn atoms, whereas there was no diffusion of electrons around the S atoms, forming a stable charge transfer process. In addition, the Gibbs free energy of H atom adsorption by CdS, ZnS, and Cd<sub>0.8</sub>Zn<sub>0.2</sub>S was calculated (Fig. 5h). The ΔG<sub>H\*</sub> value (0.22 eV) was significantly lower after the formation of the Cd<sub>0.8</sub>Zn<sub>0.2</sub>S solid solution (Fig. 5i), which was favorable for photocatalytic hydrogen production [49]. The ΔG<sub>H\*</sub> values

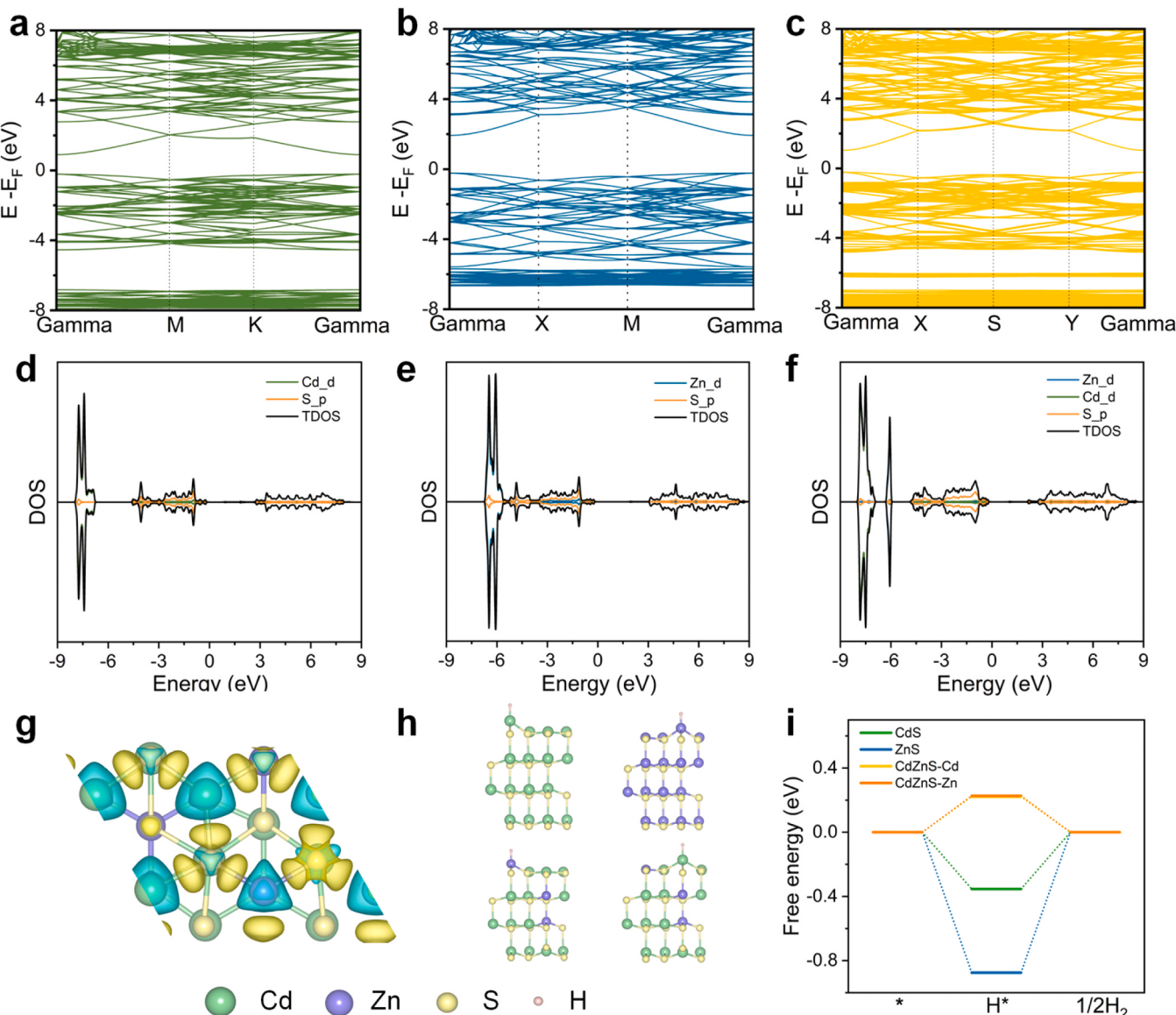


**Fig. 5.** Energy band structure (a-c) and density of states (DOS) (d-f) of the CdS, ZnS, and Cd<sub>0.8</sub>Zn<sub>0.2</sub>S. Charge density difference (g) and schematic structure model (h) of H adsorption by the Cd<sub>0.8</sub>Zn<sub>0.2</sub>S. (i) Free energy diagrams of reaction of CdS, ZnS, and Cd<sub>0.8</sub>Zn<sub>0.2</sub>S.

at active sites of CdS and ZnS were  $-0.36$  and  $-0.87$  eV, respectively, suggesting too strong adsorption of H atom on the surface that hindered hydrogen diffusion [56]. DFT results suggested that an optimal surface could be formed by the replacement of Cd sites with Zn atoms, while a lower or higher Zn concentration would lead to an insufficient number of active sites or even formation of inactive sites. With the formation of H atoms from water or protons via photoexcited electrons, the ideal adsorption and desorption environment of  $\text{Cd}_{0.8}\text{Zn}_{0.2}\text{S}$  favored the hydrogen escape from the active sites to *S. ovata*. This could be a potentially important factor resulting in the improved acetate production in the  $\text{Cd}_{0.8}\text{Zn}_{0.2}\text{S}/\text{S. ovata}$  system, as discussed in the following section.

### 3.4. Mechanism underlying photosynthetic acetate production in the $\text{Cd}_{0.8}\text{Zn}_{0.2}\text{S}/\text{S. ovata}$ system

To gain insight into the molecular mechanism underlying photocatalytic  $\text{CO}_2$  conversion, triplicate *S. ovata* cultures under photoautotrophic ( $\text{Cd}_{0.8}\text{Zn}_{0.2}\text{S}/\text{light}/\text{CO}_2$ ) and heterotrophic (betaine/ $\text{CO}_2$ ) conditions were collected for transcriptome analysis. The score plots of principal component analysis (PCA) showed that transcriptome from  $\text{Cd}_{0.8}\text{Zn}_{0.2}\text{S}$ -fed and betaine-fed *S. ovata* were clustered into discriminative groups with 95% confidence (Fig. 6a). This result suggested that the photoexcited  $\text{Cd}_{0.8}\text{Zn}_{0.2}\text{S}$  significantly affected the physiological state of *S. ovata* in the  $\text{Cd}_{0.8}\text{Zn}_{0.2}\text{S}/\text{S. ovata}$  system. The differentially expressed genes (fold change (FC)  $> 1.5$  and p value  $< 0.05$ ), including 1098 of the up-regulated and 1051 of the down-regulated, were identified in the  $\text{Cd}_{0.8}\text{Zn}_{0.2}\text{S}$ -fed group compared to the heterotrophic group (Fig. 6b and Supplementary Data S1). The Kyoto Encyclopedia of Genes and Genomes database was used for the analysis of biological pathways. The results showed that the expression of most genes associated with electron transfer, energy conversion, and  $\text{CO}_2$  fixation was significantly up-regulated in the  $\text{Cd}_{0.8}\text{Zn}_{0.2}\text{S}/\text{S. ovata}$  system, which was considered to be responsible for the photosynthesis.

In addition to the fast kinetics observed on the semiconductor

photocatalyst, the key to the operation of the biohybrid system is the interaction of the microbial catalyst with these external donors, which allows for synergistic electron harvest and carbon metabolism [6,57]. The membrane-associated proteins play important roles in direct electron transfer [43]. The up-regulated genes encoding membrane-bound flavoproteins (Fp), cytochromes, and ferredoxin (Fd) revealed that the electrons from photoexcited  $\text{Cd}_{0.8}\text{Zn}_{0.2}\text{S}$  could be transferred through these proteins into *S. ovata* for subsequent conversion of  $\text{CO}_2$  (Fig. 6c and Table S8) [58]. It was further confirmed by the results of membrane protein assay, which showed that the normalized concentrations of membrane-bound proteins in the  $\text{Cd}_{0.8}\text{Zn}_{0.2}\text{S}/\text{S. ovata}$  system significantly increased after illumination (Fig. S16). Specifically, Fp is considered to be the key membrane-integrated electron carrier and plays a major role in the electron transfer [4,58]. Cyclic voltammetry (CV) curve of *S. ovata* showed a dominant redox center with a mid-potential of  $-0.48$  V (vs. SHE), which could be assigned to Fp distributed on the cell membrane (Fig. 7a) [4,59]. Compared with pure *S. ovata*, a higher peak current of the  $\text{Cd}_{0.8}\text{Zn}_{0.2}\text{S}/\text{S. ovata}$  under illumination indicated that the  $\text{Cd}_{0.8}\text{Zn}_{0.2}\text{S}$  improved the electron transfer in the biohybrid system. The introduction of biocompatible  $\text{Cd}_{0.8}\text{Zn}_{0.2}\text{S}$  did not significantly alter the electron transfer pathway of *S. ovata*, but promoted the formation of membrane-bound redox active mediators. Furthermore, the reduction potentials of the photoexcited  $\text{Cd}_{0.8}\text{Zn}_{0.2}\text{S}$  were higher than that of the redox active mediators, ensuring that *S. ovata* could efficiently harvest photoelectrons through membrane proteins. Given Fp had a more negative redox potential than  $\text{NAD(P)}^+/\text{NAD(P)H}$  couple ( $-0.32$  V) [58], the electrons obtained by *S. ovata* could be utilized to produce the universal electron donors (NADH and NAD(P)H) for intracellular  $\text{CO}_2$  conversion.

Moreover, the genes of membrane-bound [Ni-Fe] hydrogenases and soluble [Fe-Fe] hydrogenase complex (HydABC) for hydrogen production/utilization were significantly up-regulated (Fig. 6c and Table S9) [60]. It indicated that hydrogen might act as an electron donor for cell metabolism [43,61]. The yield of photocatalytic  $\text{H}_2$  by  $\text{Cd}_{0.8}\text{Zn}_{0.2}\text{S}$  after 24 h of illumination was investigated to reach  $7.13 \pm 0.65 \text{ mmol g}^{-1}_{\text{cat}}$ .

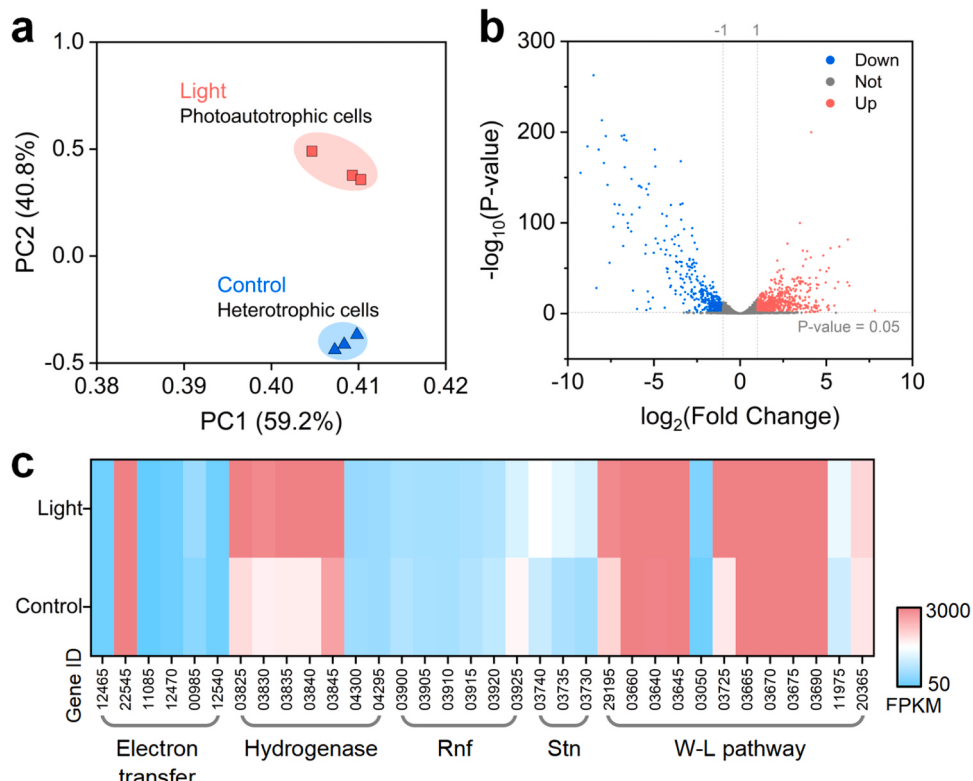
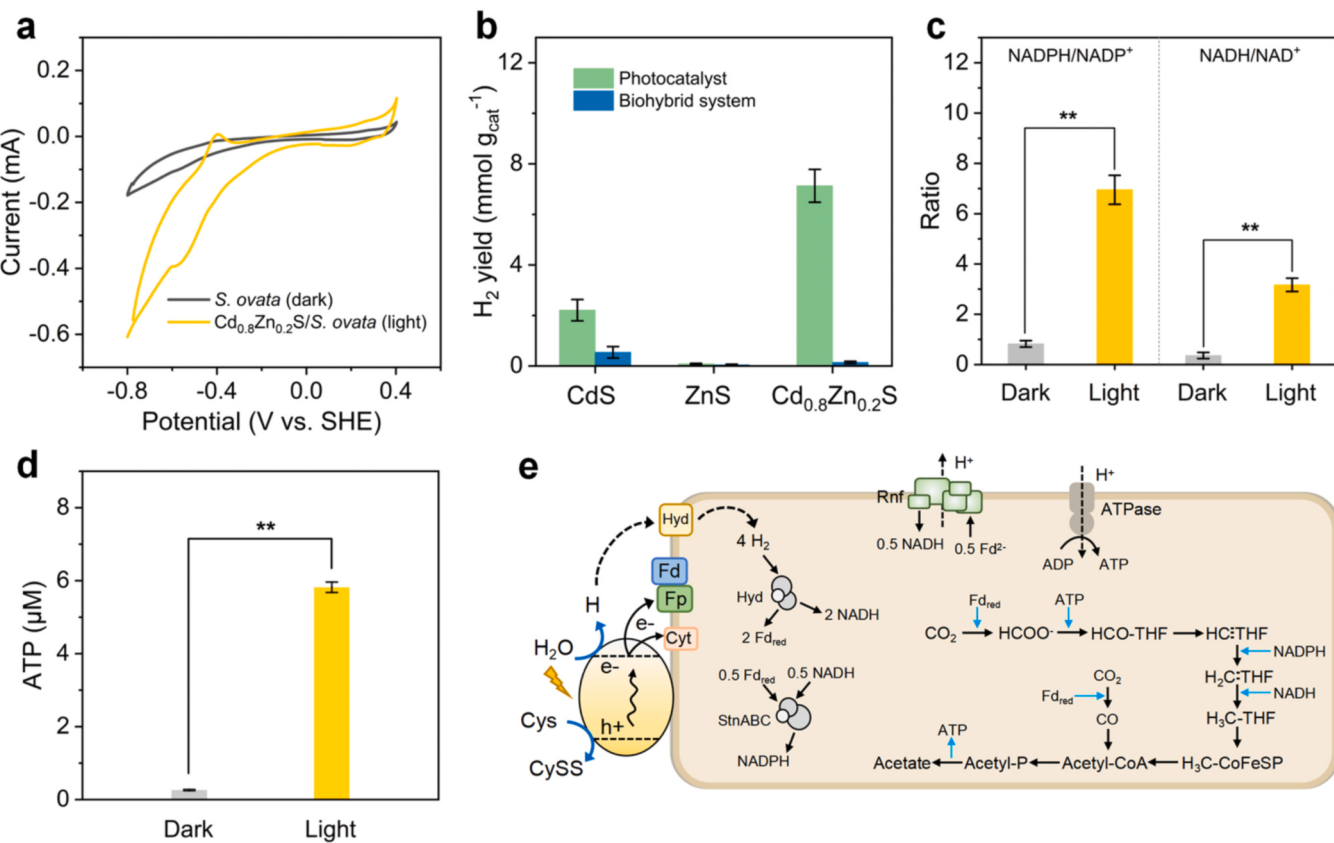


Fig. 6. PCA (a) and volcano plot (b) of the transcriptomic data. (c) Heatmaps of differentially expressed genes.



**Fig. 7.** (a) CVs of the *S. ovata* and  $\text{Cd}_{0.8}\text{Zn}_{0.2}\text{S}/\text{S. ovata}$  biohybrids in 10 mM of phosphate buffered saline solution (pH 7). (b) The initial hydrogen generation rate over CdS, ZnS, and  $\text{Cd}_{0.8}\text{Zn}_{0.2}\text{S}$  by 4 h test. NAD(P)H/NAD(P)<sup>+</sup> ratio (c) and ATP concentrations (d) in the  $\text{Cd}_{0.8}\text{Zn}_{0.2}\text{S}/\text{S. ovata}$  system under different conditions. (e) Proposed mechanism of photosynthesis in the  $\text{Cd}_{0.8}\text{Zn}_{0.2}\text{S}/\text{S. ovata}$  system. Cys: cysteine. CySS:cystine.

which was 3.2- and 83.8-fold higher than that of CdS and ZnS, respectively (Fig. 7b), suggesting the synergistic cooperation of Cd and Zn sites in  $\text{Cd}_{0.8}\text{Zn}_{0.2}\text{S}$  for high production of  $\text{H}_2$ . In contrast, a negligible  $\text{H}_2$  yield was observed in all biohybrid systems under illumination, demonstrating that the produced  $\text{H}_2$  could be harvested by *S. ovata* for  $\text{CO}_2$  reduction. However,  $\text{H}_2$  cannot be completely consumed by *S. ovata* due to its low solubility and high utilized concentration threshold [45, 62]. According to the optimal binding energy of H atom at active sites of  $\text{Cd}_{0.8}\text{Zn}_{0.2}\text{S}$  and the tight bonding of  $\text{Cd}_{0.8}\text{Zn}_{0.2}\text{S}$  and *S. ovata*, the formed H atoms on the surface of photoexcited  $\text{Cd}_{0.8}\text{Zn}_{0.2}\text{S}$  could be effectively transferred from active sites to *S. ovata* for  $\text{CO}_2$  reduction, thus avoiding  $\text{H}_2$  evolution as a side reaction [45].

The H atoms transferred from active sites of  $\text{Cd}_{0.8}\text{Zn}_{0.2}\text{S}$  or possibly a small amount of produced  $\text{H}_2$  drove the simultaneous reduction of Fd and  $\text{NAD}^+$  to  $\text{Fd}_{\text{red}}$  and NADH, respectively, through hydrogenases. Subsequently, the overexpressed Nfn-type transhydrogenase (Stn complex) catalyzed the electron bifurcation from  $\text{Fd}_{\text{red}}$  and NADH to NADP<sup>+</sup> (Fig. 6c and Table S10). In addition, the  $\text{Fd}_{\text{red}}$  could be used by the ferredoxin:NAD<sup>+</sup> oxidoreductase (Rnf complex) for the reduction of  $\text{NAD}^+$ , thereby generating a  $\text{H}^+$ -gradient across the membrane for ATP generation (Fig. 6c and Table S10). As expected, the increased NAD(P)H/NAD(P)<sup>+</sup> ratio and ATP concentration were detected in the  $\text{Cd}_{0.8}\text{Zn}_{0.2}\text{S}/\text{S. ovata}$  system under illumination (Fig. 7c,d). The generated intracellular electron donors and ATP could drive the  $\text{CO}_2$  fixation pathway of *S. ovata* for  $\text{CO}_2$  reduction. Specifically, all necessary enzymes in the Wood-Ljungdahl (W-L) pathway for  $\text{CO}_2$  fixation were significantly up-regulated in the  $\text{Cd}_{0.8}\text{Zn}_{0.2}\text{S}/\text{S. ovata}$  system (Fig. 6c and Table S11), which supported a high yield of acetate through photosynthesis.

The reactive oxygen species (ROS) generated under illumination is an important factor affecting the bacterial viability in the biohybrid

systems [44]. It was found that the genes encoding superoxide dismutase and catalase [63] were up-regulated, which activated a survival response to the ROS stress of *S. ovata* in the  $\text{Cd}_{0.8}\text{Zn}_{0.2}\text{S}/\text{S. ovata}$  system (Table S12). Furthermore, the ROS levels in the cytoplasm of *S. ovata* were tested through a ROS assay kit. The result showed that the ROS concentration in pure *S. ovata* was 2.6 times higher than that in  $\text{Cd}_{0.8}\text{Zn}_{0.2}\text{S}/\text{S. ovata}$  after illumination for 24 h (Fig. S17). This revealed the beneficial effect of  $\text{Cd}_{0.8}\text{Zn}_{0.2}\text{S}$  on eliminating ROS, which might be attributed to its multiple energy levels that promoted the neutralization of the active species to stable states [64]. These results confirmed that the cells integrated with  $\text{Cd}_{0.8}\text{Zn}_{0.2}\text{S}$  possessed a stronger resistance to oxidative damage compared to pure *S. ovata*, contributing to the long running time of the  $\text{Cd}_{0.8}\text{Zn}_{0.2}\text{S}/\text{S. ovata}$  system.

Conclusively, the pathways for electron and proton transfer toward acetate production in the  $\text{Cd}_{0.8}\text{Zn}_{0.2}\text{S}/\text{S. ovata}$  system were proposed (Fig. 7e). Initially, the  $\text{Cd}_{0.8}\text{Zn}_{0.2}\text{S}$  was excited to produce the electron-hole pairs under visible light. Due to the presence of twin-induced homojunctions, the photogenerated electrons and holes could be spatially transferred to the ZB and WZ regions, respectively, thus effectively separating the photogenerated electron-hole pairs. The holes were subsequently quenched through the oxidation of cysteine. The conduction band electrons might be transferred to *S. ovata* via hydrogen- and membrane-bound protein-mediated electron transport pathways, thereby generating excessive intracellular electron donors. In addition, ATP synthesis was driven by the proton motive force generated through the transmembrane Rnf complex. Finally, the resulted high energy reducing equivalents and ATP were passed on to the W-L pathway for efficient synthesis of acetate from  $\text{CO}_2$  conversion.

#### 4. Conclusions

In conclusion, twinning  $\text{Cd}_{0.8}\text{Zn}_{0.2}\text{S}$  solid solutions with dense distribution of homojunctions were synthesized and explored as efficient photosensitizers in the biohybrid system. The designed  $\text{Cd}_{0.8}\text{Zn}_{0.2}\text{S}/\text{S. ovata}$  system achieved the highest photosynthetic acetate production of  $49.33 \pm 3.54 \text{ mM}$  at the production rate of  $8.22 \pm 0.59 \text{ mM d}^{-1}$  and the quantum efficiency of  $16.82 \pm 1.21\%$ . This was attributed to the close interconnection of the zinc-blende and wurtzite phases at the atomic level in the  $\text{Cd}_{0.8}\text{Zn}_{0.2}\text{S}$ , which showed significant advantages in efficient separation of photogenerated electron-hole pairs and prevention of photocorrosion. Furthermore, it was found that indirect and direct electron uptake mediated by hydrogen and membrane-bound proteins (such as cytochromes, ferredoxin, and flavoproteins), respectively, contributed to photoelectron transfer from  $\text{Cd}_{0.8}\text{Zn}_{0.2}\text{S}$  to *S. ovata* for  $\text{CO}_2$  conversion. This work paves a convenient route to design efficient photocatalyst with twin-induced homojunctions for construction of biohybrid systems, and provides insight into the complex interactions between semiconductors and microorganisms.

#### CRediT authorship contribution statement

**Kejing Zhang:** Investigation, Data curation, Writing – original draft.  
**Ruijie Li:** Formal analysis, Investigation, Data curation, Software.  
**Jianxin Chen:** Investigation, Data curation, Writing – review & editing.  
**Liyuan Chai:** Supervision, Funding acquisition. **Zhang Lin:** Validation, Writing – review & editing. **Long Zou:** Investigation, Data curation, Writing – review & editing. **Yan Shi:** Conceptualization, Funding acquisition, Writing – review & editing.

#### Declaration of Competing Interest

The authors declare that they have no known competing financial interests or personal relationships that could have appeared to influence the work reported in this paper.

#### Data Availability

Data will be made available on request.

#### Acknowledgments

This work was supported by the National Natural Science Foundation of China (Nos. 42177231 and 21836002), National Key Research and Development Program of China (Nos. SQ2019YFC180057 and 2019YFA0210400), Major Program Natural Science Foundation of Hunan Province of China (No. 2021JC0001), and the Natural Science Foundation of Jiangxi Province (No. 20202ACB215001) for their financial support.

#### Appendix A. Supporting information

Supplementary data associated with this article can be found in the online version at [doi:10.1016/j.apcatb.2023.123375](https://doi.org/10.1016/j.apcatb.2023.123375).

#### References

- [1] P. Zhu, Z.-Y. Wu, A. Elgazzar, C. Dong, T.-U. Wi, F.-Y. Chen, Y. Xia, Y. Feng, M. Shakouri, J.Y. Kim, Z. Fang, T.A. Hatton, H. Wang, Continuous carbon capture in an electrochemical solid-electrolyte reactor, *Nature* 618 (2023) 959–966.
- [2] C. Tian, J. Lv, W. Zhang, H. Wang, J. Chao, L. Chai, Z. Lin, Accelerated degradation of microplastics at the liquid interface of ice crystals in frozen aqueous solutions, *Angew. Chem. -Int. Ed.* 61 (2022), e202206947.
- [3] A.W.D. Larkum, Limitations and prospects of natural photosynthesis for bioenergy production, *Curr. Opin. Biotechnol.* 21 (2010) 271–276.
- [4] N. Kornienko, K.K. Sakimoto, D.M. Herlihy, S.C. Nguyen, A.P. Alivisatos, C. B. Harris, A. Schwartzberg, P. Yang, Spectroscopic elucidation of energy transfer in hybrid inorganic-biological organisms for solar-to-chemical production, *Proc. Natl. Acad. Sci. U. S. A.* 113 (2016) 11750–11755.
- [5] D. Kim, K.K. Sakimoto, D. Hong, P. Yang, Artificial photosynthesis for sustainable fuel and chemical production, *Angew. Chem. -Int. Ed.* 54 (2015) 3259–3266.
- [6] X. Fang, S. Kalathil, E. Reisner, Semi-biological approaches to solar-to-chemical conversion, *Chem. Soc. Rev.* 49 (2020) 4926–4952.
- [7] B. Han, X. Ou, Z. Deng, Y. Song, C. Tian, H. Deng, Y.-J. Xu, Z. Lin, Nickel Metal-organic framework monolayers for photoreduction of diluted  $\text{CO}_2$ : Metal-node-dependent activity and selectivity, *Angew. Chem. -Int. Ed.* 57 (2018) 16811–16815.
- [8] H. Song, X. Ou, B. Han, H. Deng, W. Zhang, C. Tian, C. Cai, A. Lu, Z. Lin, L. Chai, An overlooked natural hydrogen evolution pathway:  $\text{Ni}^{2+}$  boosting  $\text{H}_2\text{O}$  reduction by  $\text{Fe}(\text{OH})_2$  oxidation during low-temperature serpentinization, *Angew. Chem. -Int. Ed.* 60 (2021) 24054–24058.
- [9] L. Fu, Z. Qu, L. Zhou, Y. Ding, Boosting electrochemical  $\text{CO}_2$  reduction to  $\text{CO}$  over interfacial hydroxide-metal catalysts, *Appl. Catal. B-Environ.* 339 (2023), 123170.
- [10] K.K. Sakimoto, A.B. Wong, P. Yang, Self-sensitization of nonphotosynthetic bacteria for solar-to-chemical production, *Science* 351 (2016) 74–77.
- [11] S. Fang, M. Rahaman, J. Bharti, E. Reisner, M. Robert, G.A. Ozin, Y.H. Hu, Photocatalytic  $\text{CO}_2$  reduction, *Nat. Rev. Methods Prim.* 3 (2023) 61.
- [12] O. Bachar, R. Cohen, M.M. Meirovich, Y. Cohen, O. Yehezkel, Biotic-abiotic hybrids for bioanalytics and biocatalysis, *Curr. Opin. Biotechnol.* 81 (2023), 102943.
- [13] J. Zhang, L. Liu, X. Chen, Pushing hybrids to the limits, *Nat. Catal.* 5 (2022) 975–976.
- [14] J. Ye, J. Yu, Y. Zhang, M. Chen, X. Liu, S. Zhou, Z. He, Light-driven carbon dioxide reduction to methane by *Methanoscincus barkeri*- $\text{CdS}$  biohybrid, *Appl. Catal. B-Environ.* 257 (2019), 117916.
- [15] M. Martins, C. Toste, I.A.C. Pereira, Enhanced light-driven hydrogen production by self-sensitized biohybrid systems, *Angew. Chem. -Int. Ed.* 60 (2021) 9055–9062.
- [16] Z. Peng, Y. Su, M. Siaj, Encapsulation of tin oxide layers on gold nanoparticles decorated one-dimensional  $\text{CdS}$  nanoarrays for pure Z-scheme photoanodes towards solar hydrogen evolution, *Appl. Catal. B-Environ.* 330 (2023), 122614.
- [17] X. Xiang, L. Zhang, C. Luo, J. Zhang, B. Cheng, G. Liang, Z. Zhang, J. Yu, Ultrafast electron transfer from  $\text{CdS}$  quantum dots to atomically-dispersed Pt for enhanced  $\text{H}_2$  evolution and value-added chemical synthesis, *Appl. Catal. B-Environ.* 340 (2024), 123196.
- [18] Q. Li, B. Guo, J. Yu, J. Ran, B. Zhang, H. Yan, J.R. Gong, Highly efficient visible-light-driven photocatalytic hydrogen production of  $\text{CdS}$ -cluster-decorated graphene nanosheets, *J. Am. Chem. Soc.* 133 (2011) 10878–10884.
- [19] P. Gai, W. Yu, H. Zhao, R. Qi, F. Li, L. Liu, F. Lv, S. Wang, Solar-powered organic semiconductor-bacteria biohybrids for  $\text{CO}_2$  reduction into acetic acid, *Angew. Chem. -Int. Ed.* 59 (2020) 7224–7229.
- [20] L. Goebels, A. Poehlein, A. Dummitt, R. Egelkamp, C. Kroeger, J. Haerdter, T. Hackl, A. Feld, H. Weller, R. Daniel, W.R. Streit, M.C. Schoelmerich, Cysteine: an overlooked energy and carbon source, *Sci. Rep.* 11 (2021) 2139.
- [21] Z. Mei, B. Zhang, J. Zheng, S. Yuan, Z. Zhuo, X. Meng, Z. Chen, K. Amine, W. Yang, L.-W. Wang, W. Wang, S. Wang, Q. Gong, J. Li, F.-S. Liu, F. Pan, Tuning Cu dopant of  $\text{Zn}_{0.5}\text{Cd}_{0.5}\text{S}$  nanocrystals enables high-performance photocatalytic  $\text{H}_2$  evolution from water splitting under visible-light irradiation, *Nano Energy* 26 (2016) 405–416.
- [22] Q. Zhu, Q. Xu, M. Du, X. Zeng, G. Zhong, B. Qiu, J. Zhang, Recent progress of metal sulfide photocatalysts for solar energy conversion, *Adv. Mater.* 34 (2022), 2202929.
- [23] S. Yoshino, T. Takayama, Y. Yamaguchi, A. Iwase, A. Kudo,  $\text{CO}_2$  reduction using water as an electron donor over heterogeneous photocatalysts aiming at artificial photosynthesis, *Acc. Chem. Res.* 55 (2022) 966–977.
- [24] G. Zuo, Y. Wang, W.L. Teo, A. Xie, Y. Guo, Y. Dai, W. Zhou, D. Jana, Q. Xian, W. Dong, Y. Zhao, Ultrathin  $\text{ZnIn}_2\text{S}_4$  nanosheets anchored on  $\text{Ti}_3\text{C}_2\text{TX}$  MXene for photocatalytic  $\text{H}_2$  evolution, *Angew. Chem. -Int. Ed.* 59 (2020) 11287–11292.
- [25] J. Ran, G. Gao, F.-T. Li, T.-Y. Ma, A. Du, S.-Z. Qiao,  $\text{Ti}_3\text{C}_2$  MXene co-catalyst on metal sulfide photo-absorbers for enhanced visible-light photocatalytic hydrogen production, *Nat. Commun.* 8 (2017) 13907.
- [26] M. Liu, D. Jing, Z. Zhou, L. Guo, Twin-induced one-dimensional homojunctions yield high quantum efficiency for solar hydrogen generation, *Nat. Commun.* 4 (2013) 2278.
- [27] S. Sun, X. Zhang, J. Cui, Q. Yang, S. Liang, Twin engineering of photocatalysts: a minireview, *Catal. Sci. Technol.* 10 (2020) 4164–4178.
- [28] M. Liu, L. Wang, G. Lu, X. Yao, L. Guo, Twins in  $\text{Cd}_{1-x}\text{Zn}_x\text{S}$  solid solution: highly efficient photocatalyst for hydrogen generation from water, *Energy Environ. Sci.* 4 (2011) 1372–1378.
- [29] H. Du, K. Liang, C.-Z. Yuan, H.-L. Guo, X. Zhou, Y.-F. Jiang, A.-W. Xu, Bare  $\text{Cd}_{1-x}\text{Zn}_x\text{S}$  ZB/WZ heterophase nanojunctions for visible light photocatalytic hydrogen production with high efficiency, *ACS Appl. Mater. Interfaces* 8 (2016) 24550–24558.
- [30] B.-J. Ng, L.K. Putri, X.Y. Kong, K.P.Y. Shak, P. Pasbakhsh, S.-P. Chai, A. R. Mohamed, Sub-2nm Pt-decorated  $\text{Zn}_{0.5}\text{Cd}_{0.5}\text{S}$  nanocrystals with twin-induced homojunctions for efficient visible-light-driven photocatalytic  $\text{H}_2$  evolution, *Appl. Catal. B-Environ.* 224 (2018) 360–367.
- [31] L. Lu, Y.F. Shen, X.H. Chen, L.H. Qian, K. Lu, Ultrahigh strength and high electrical conductivity in copper, *Science* 304 (2004) 422–426.
- [32] B. Weng, M.-Y. Qi, C. Han, Z.-R. Tang, Y.-J. Xu, Photocorrosion inhibition of semiconductor-based photocatalysts: Basic principle, current development, and future perspective, *ACS Catal.* 9 (2019) 4642–4687.

- [33] H.-B. Huang, Z.-B. Fang, K. Yu, J. Lu, R. Cao, Visible-light-driven photocatalytic H<sub>2</sub> evolution over CdZnS nanocrystal solid solutions: interplay of twin structures, sulfur vacancies and sacrificial agents, *J. Mater. Chem. A* 8 (2020) 3882–3891.
- [34] K.P. Nevin, T.L. Woodard, A.E. Franks, Z.M. Summers, D.R. Lovley, Microbial electrosynthesis: Feeding microbes electricity to convert carbon dioxide and water to multicarbon extracellular organic compounds, *Mbio* 1 (2010) e00103–00110.
- [35] L. Chen, P.-L. Tremblay, S. Mohanty, K. Xu, T. Zhang, Electrosynthesis of acetate from CO<sub>2</sub> by a highly structured biofilm assembled with reduced graphene oxide-tetraethylene pentamine, *J. Mater. Chem. A* 4 (2016) 8395–8401.
- [36] Y. Su, S. Cestellos-Blanco, J.M. Kim, Y.-X. Shen, Q. Kong, D. Lu, C. Liu, H. Zhang, Y. Cao, P. Yang, Close-packed nanowire-bacteria hybrids for efficient solar-driven CO<sub>2</sub> Fixation, *Joule* 4 (2020) 800–811.
- [37] S. Jin, Y. Jeon, M.S. Jeon, J. Shin, Y. Song, S. Kang, J. Bae, S. Cho, J.-K. Lee, D. R. Kim, B.-K. Cho, Acetogenic bacteria utilize light-driven electrons as an energy source for autotrophic growth, *Proc. Natl. Acad. Sci. U. S. A.* 118 (2021), e2020552118.
- [38] Y. Liu, Y. Ma, W. Liu, Y. Shang, A. Zhu, P. Tan, X. Xiong, J. Pan, Facet and morphology dependent photocatalytic hydrogen evolution with CdS nanoflowers using a novel mixed solvothermal strategy, *J. Colloid Interface Sci.* 513 (2018) 222–230.
- [39] J. Song, H. Zhao, R. Sun, X. Li, D. Sun, An efficient hydrogen evolution catalyst composed of palladium phosphorous sulphide (PdP similar to 0.33S similar to 1.67) and twin nanocrystal Zn<sub>0.5</sub>Cd<sub>0.5</sub>S solid solution with both homo- and heterojunctions, *Energy Environ. Sci.* 10 (2017) 225–235.
- [40] X. Zong, H. Yan, G. Wu, G. Ma, F. Wen, L. Wang, C. Li, Enhancement of photocatalytic H<sub>2</sub> evolution on CdS by loading MoS<sub>2</sub> as cocatalyst under visible light irradiation, *J. Am. Chem. Soc.* 130 (2008) 7176.
- [41] S. Chandrasekaran, L. Yao, L. Deng, C. Bowen, Y. Zhang, S. Chen, Z. Lin, F. Peng, P. Zhang, Recent advances in metal sulfides: from controlled fabrication to electrocatalytic, photocatalytic and photoelectrochemical water splitting and beyond, *Chem. Soc. Rev.* 48 (2019) 4178–4280.
- [42] D. Liu, Z. Su, B. Han, K. Xia, C. Zhou, Q. Gao, Cobalt–aluminum oxide clusters-embedded  $\gamma$ -Al<sub>2</sub>O<sub>3</sub> nanosheets for peroxymonosulfate activation: Interfacial pH-buffering property to eliminate cobalt leaching and boost the catalytic activity, *Appl. Catal. B-Environ.* 330 (2023), 122555.
- [43] J. Madjarov, R. Soares, C.M. Paquete, R.O. Louro, *Sporomusa ovata* as catalyst for bioelectrochemical carbon dioxide reduction: A review across disciplines from microbiology to process engineering, *Front. Microbiol.* 13 (2022), 913311.
- [44] H. Zhang, H. Liu, Z. Tian, D. Lu, Y. Yu, S. Cestellos-Blanco, K.K. Sakimoto, P. Yang, Bacteria photosensitized by intracellular gold nanoclusters for solar fuel production, *Nat. Nanotechnol.* 13 (2018) 900–905.
- [45] J. Ye, C. Wang, C. Gao, T. Fu, C. Yang, G. Ren, J. Lü, S. Zhou, Y. Xiong, Solar-driven methanogenesis with ultrahigh selectivity by turning down H<sub>2</sub> production at biotic-abiotic interface, *Nat. Commun.* 13 (2022) 6612.
- [46] B. Baral, K. Parida, {040/110} facet isotype heterojunctions with monoclinic scheelite BiVO<sub>4</sub>, *Inorg. Chem.* 59 (2020) 10328–10342.
- [47] H. Xu, W. Fan, Y. Zhao, B. Chen, Y. Gao, X. Chen, D. Xu, W. Shi, Amorphous iron (III)-borate decorated electrochemically treated-BiVO<sub>4</sub> photoanode for efficient photoelectrochemical water splitting, *Chem. Eng. J.* 411 (2021), 128480.
- [48] Z.-X. Yang, P. Zhang, W. Zhong, Y. Deng, C.-T. Au, Y.-W. Du, Design, growth, and characterization of morphology-tunable Cd<sub>x</sub>Zn<sub>1-x</sub>S nanostructures generated by a one-step thermal evaporation process, *Crystengcomm* 14 (2012) 4298–4305.
- [49] H. Gu, H. Zhang, X. Wang, Q. Li, S. Chang, Y. Huang, L. Gao, Y. Cui, R. Liu, W.-L. Dai, Robust construction of CdSe nanorods@Ti<sub>3</sub>C<sub>2</sub> MXene nanosheet for superior photocatalytic H<sub>2</sub> evolution, *Appl. Catal. B-Environ.* 328 (2023), 122537.
- [50] Y. Zhong, G. Zhao, F. Ma, Y. Wu, X. Hao, Utilizing photocorrosion-recrystallization to prepare a highly stable and efficient CdS/WS<sub>2</sub> nanocomposite photocatalyst for hydrogen evolution, *Appl. Catal. B-Environ.* 199 (2016) 466–472.
- [51] F.Y. Yan, R. Noufi, M.M. Al-Jassim, Grain-boundary physics in polycrystalline CuInSe<sub>2</sub> revisited: experiment and theory, *Phys. Rev. Lett.* 96 (2006), 205501.
- [52] Burke Perdew Emzerhof, Generalized Gradient Approximation Made Simple, *Phys. Rev. Lett.* 77 (1996) 3865–3868.
- [53] E. Blanchet, F. Duquenne, Y. Rafrati, L. Etcheverry, B. Erable, A. Bergel, Importance of the hydrogen route in up-scaling electrosynthesis for microbial CO<sub>2</sub> reduction, *Energy Environ. Sci.* 8 (2015) 3731–3744.
- [54] D.G. Davis, E. Blanco, An electrochemical study of the oxidation of L-cysteine, *J. Electroanal. Chem.* 12 (1966) 254–260.
- [55] M. Liu, Y. Chen, J. Su, J. Shi, X. Wang, L. Guo, Photocatalytic hydrogen production using twinned nanocrystals and an unanchored NiS<sub>x</sub> co-catalyst, *Nat. Energy* 1 (2016) 16151.
- [56] J. Ye, C. Wang, C. Gao, T. Fu, C. Yang, G. Ren, J. Lu, S. Zhou, Y. Xiong, Solar-driven methanogenesis with ultrahigh selectivity by turning down H<sub>2</sub> production at biotic-abiotic interface, *Nat. Commun.* 13 (2022) 6612.
- [57] Y. Jiang, B. Tian, Inorganic semiconductor biointerfaces, *Nat. Rev. Mater.* 3 (2018) 473–490.
- [58] F. Kracke, I. Vassilev, J.O. Kroemer, Microbial electron transport and energy conservation—the foundation for optimizing bioelectrochemical systems, *Front. Microbiol.* 6 (2015) 575.
- [59] W. Kuhn, G. Gottschalk, Characterization of the cytochromes occurring in *Methanosarcina* species, *Eur. J. Biochem.* 135 (1983) 89–94.
- [60] F. Kremp, J. Roth, V. Mueller, The *Sporomusa* type Nfn is a novel type of electron-bifurcating transhydrogenase that links the redox pools in acetogenic bacteria, *Sci. Rep.* 10 (2020) 14872.
- [61] N. Aryal, P.-L. Tremblay, D.M. Lizak, T. Zhang, Performance of different *Sporomusa* species for the microbial electrosynthesis of acetate from carbon dioxide, *Bioresour. Technol.* 233 (2017) 184–190.
- [62] X. Guan, X. Hu, T.L. Atallah, Y. Xie, S. Lu, B. Cao, J. Sun, K. Wu, Y. Huang, X. Duan, J.R. Caram, Y. Yu, J.O. Park, C. Liu, S. Ersan, Maximizing light-driven CO<sub>2</sub> and N<sub>2</sub> fixation efficiency in quantum dot-bacteria hybrids, *Nat. Catal.* 5 (2022) 1019.
- [63] E.D. Coulter, D.M. Kurtz, A role for rubredoxin in oxidative stress protection in *Desulfovibrio vulgaris*: catalytic electron transfer to rubrerythrin and two-iron superoxide reductase, *Arch. Biochem. Biophys.* 394 (2001) 76–86.
- [64] Y. Gao, N. Shao, Y. Pei, Z. Chen, X.C. Zeng, Catalytic activities of subnanometer gold clusters (Au-16-Au-18, Au-20, and Au-27-Au-35) for CO oxidation, *Acs Nano* 5 (2011) 7818–7829.